Separation and Purification Technology 307 (2023) 122824

Contents lists available at ScienceDirect

Separation and Purification Technology

journal homepage: www.elsevier.com/locate/seppur

A novel cryogenic fixed-bed adsorption apparatus for studying green hydrogen recovery from natural gas grids

Lucas F.A.S. Zafanelli [a,b,c,d], Ezzeldin Aly [a,b], Alírio E. Rodrigues [c,d], José A.C. Silva [a,b]

[a] Centro de Investigação de Montanha (CIMO), Instituto Politécnico de Bragança, Campus Santa Apolónia, 5300-253 Bragança, Portugal
[b] Laboratório Associado para a Sustentabilidade e Tecnologia em Regiões de Montanha (SusTEC), Instituto Politécnico de Bragança, Campus de Santa Apolónia, 5300-253 Bragança, Portugal
[c] Laboratory of Separation and Reaction Engineering (LSRE), Associate Laboratory LSRE/LCM, Department of Chemical Engineering, Faculty of Engineering, University of Porto, 4099-002 Porto, Portugal
[d] Associate Laboratory in Chemical Engineering (ALiCE), Faculdade de Engenharia, Universidade do Porto, Rua Dr. Roberto Frias, 4200-465 Porto, Portugal

ARTICLE INFO

Keywords:
Binder-free zeolite 13X
Green Hydrogen
Cryogenic fixed bed adsorption
Natural gas grids
Numerical modeling

ABSTRACT

In this work, a fixed-bed adsorption apparatus was developed to carry out adsorption breakthrough curve experiments at cryogenic temperatures (between 195 and 273 K) and high pressures (up to 18 bar) to screen adsorbents for the dynamic separation of green hydrogen blended in natural gas grids. Therefore, a series of breakthrough curve experiments of single component CH_4 and H_2, and their mixtures on the benchmark binder-free zeolite 13X were performed. The equilibrium data obtained were fitted with the virial, dual-site Langmuir, and Langmuir isotherm models. Moreover, the equilibrium data and the isosteric heat of adsorption were compared with the data available in the literature obtained by microcalorimetric, gravimetric, and volumetric methods. The maximum loading obtained for CH_4 and H_2 at 195 K and 12 bar was 6.95 and 2.08 mol kg^{-1}. The selectivity predicted by the extended dual-site Langmuir was 17.3 for CH_4 over H_2 at 195 K and 12 bar, considering a binary interaction of a mixture of CH_4/H_2 (80/20 vol%). Additionally, binary experiments were performed to evaluate the dynamic separation of H_2 and CH_4 at the mixture ratio H_2/CH_4 (20/80 % vol.), and data was simulated by using a proper dynamic fixed-bed adsorption mathematical model. Overall, the results pointed out that the novel apparatus provides a reliable tool to collect equilibrium and dynamic information for screening adsorbents targeting the separation of green H_2 blended into natural gas grids.

1. Introduction

Green hydrogen (GH) produced from renewable energy can be a key factor in keeping global warming below 2 °C in the coming 30 years. The term "Green Hydrogen" is due to its production being free of carbon emissions, i.e., its production comes from water electrolysis powered by renewable energy sources namely sources solar, wind, hydroelectricity, or biomass. Today, almost 95 % of hydrogen production comes from steam methane reforming and coal gasification paths which generate annually about 830 Mt of CO_2 and cost approximately US$1.21–1.47 kg^{-1} [1–3]. To minimize the carbon release from these pathways, a carbon capture system has been coupled into the process, however, it increases twice the production cost [4]. From the environmental point of view, GH is crucial to achieving a sustainable energy economy. Although the price of GH is relatively higher than the others (US$3.50–6.00 kg^{-1}) [4], it is expected to decrease over the years considering the current investments in its valorization. A recent forecast indicated an investment of $500 billion through 2030 to accelerate GH deployment [5].

Hydrogen has proven attributes that make it largely regarded as a potential cost-effective clean fuel of the future [6]. For example, hydrogen is the element with the lowest molecular weight (2.016 u) and with the highest known energy content of any fuel, it is sustainable and non-toxic. Moreover, its gravimetric heat of combustion is almost three times higher than gasoline (120 MJ/kg vs 44.5 MJ/kg) and its combustion is environmentally friendly with water as the only exhaust product at conversion to energy [7]. Additionally, hydrogen can store surplus renewable power when the grid cannot soak it, and help to decarbonize heavy industry and long-distance transport (shipping for example) [2,4,8].

One of the challenges facing GH valorization is its transportation. There are at least three ways to perform the global transport of GH, namely, trucks, pipelines, and ships. The pipeline option is considered the cheapest (about USD 0.1/kg per 500 km) way to transport GH even

E-mail addresses: zafanelli@ipb.pt (L.F.A.S. Zafanelli), jsilva@ipb.pt (J.A.C. Silva).

https://doi.org/10.1016/j.seppur.2022.122824
Received 20 September 2022; Received in revised form 16 November 2022; Accepted 28 November 2022
Available online 5 December 2022

Nomenclature

a_p	Specific area of the pellet (m^{-1})
a_c	Specific area of the column (m^{-1})
b_i	Adsorption equilibrium constant of component i (bar^{-1})
$b_{\infty,i}$	Pre-exponential factor of the affinity constant at infinite temperature of component i (bar^{-1})
C	Total gas concentration ($mol{\cdot}m^{-3}$)
C_f	Feed gas concentration ($mol{\cdot}m^{-3}$)
C_{pg}	Heat capacity of gas ($J{\cdot}mol^{-1}{\cdot}K^{-1}$)
C_{ps}	Heat capacity of solid ($J{\cdot}mol^{-1}{\cdot}K^{-1}$)
d_b	Beads diameter (m)
d_c	Column diameter (m)
D_{ax}	Axial mass dispersion coefficient ($m^2{\cdot}s^{-1}$)
D_m	Molecular diffusivity ($m^2{\cdot}s^{-1}$)
F	Total molar flux ($mol{\cdot}m^{-2}{\cdot}s^{-1}$)
h_p	Film heat transfer coefficient ($W{\cdot}m^{-2}{\cdot}K^{-1}$)
h_w	Wall heat transfer coefficient ($W{\cdot}m^{-2}{\cdot}K^{-1}$)
K_{LDF}	Linear Driving Force coefficient (s^{-1})
K_{ax}	Effective axial bed thermal conductivity ($W{\cdot}m^{-1}{\cdot}K^{-1}$)
L	Length of column (m)
M_i	Molecular weight of component i ($kg{\cdot}kmol^{-1}$)
m_{ads}	Mass of adsorbent (kg)
p_i	Partial pressure of component i (bar)
P	Total pressure of column (bar)
$\overline{q}_i$	Average adsorbed phase concentration of component i ($mol{\cdot}kg^{-1}$)
q^*	Equilibrium adsorbed concentration of component ($mol{\cdot}kg^{-1}$)
q_m	Maximum adsorbed phase concentration ($mol{\cdot}kg^{-1}$)
R	Universal gas constant ($J{\cdot}mol^{-1}{\cdot}K^{-1}$)
t	Time (s)
T	Temperature in bulk gas phase (K)
T_s	Temperature in solid phase (K)
T_w	Column wall temperature (K)
v_i	Interstitial velocity ($m{\cdot}s^{-1}$)
y_i	Molar fraction of component i (-)
z	Axial coordinate in bed (m)

Greek Letters

ΔH_i	Heat adsorption of species i ($J{\cdot}mol^{-1}$)
ΔH_{st}	Isosteric heat adsorption ($J{\cdot}mol^{-1}$)
ε_b	Bed porosity
ε_p	Particle porosity
ρ_p	Solid Density ($kg{\cdot}m^{-3}$)
ρ_s	Apparent adsorbent density ($kg{\cdot}m^{-3}$)
ρ_b	Bulk density ($kg{\cdot}m^{-3}$)

for short and long-distance (up to 5000 km) compared to the other types [5]. We should note that this estimated price does not include the cost to build new pipeline infrastructure. In this way, the co-transport of GH in the existing natural gas (NG) networks is an interesting option and has been proposed, to avoid infrastructure investments [9–11]. However, one time that the GH is injected into the NG grids we need to extract it and purify it to a high grade to be able to use pure GH and NG separately when needed. For example, to convert GH into electricity by fuel cells, its quality must be about 99.97 % [12]. In this view, NG/GH separation technology needs to be developed to provide H_2 and NG with sufficient purity to be consumed.

To date, pressure swing adsorption (PSA) processes are widely used for the purification of H_2 from steam methane reforming (SMR), which can achieve purities up to 99.9999 vol% [13–15]. Also, PSA and its variations (Temperature/Vacuum/Electrification Swing Adsorption) are a mature growing technology applied to biogas upgrading [16,17] and carbon dioxide capture processes [18–20]. The conventional PSA works very well for purifying H_2 from an SMR production due to the high concentration of H_2 in the feed (>70 %) and also the operational conditions (20–50 °C and 10–50 atm) provide a great driving force to adsorb the impurities (CH_4, CO_2, CO, and H_2S), using the commercial adsorbents (e.g. 5A/13X zeolites, silica, and activated carbon). However, the allowed amount of H_2 that can be injected into the NG pipelines for distribution is limited to 10–20 % [21,22], which makes the H_2/NG separation for the standard application of a conventional H_2 PSA a challenge. For example, in this case, the amount of CH_4 can be rich up to 80 % resulting in a fast adsorbent saturation, which leads to poor recovery of H_2. Additionally, a higher number of adsorbents bed need to be used to achieve H_2 purity higher than 99.97 %, which results in an overall cost increase.

In this view, to re-use PSA technologies as a solution, one would need an adsorbent material that has a bigger CH_4 capacity than the currently available material. Thus, screening new adsorbents capable of adsorbing large quantities of CH_4 at moderate cryogenic conditions (>-42 °C) while rejecting H_2 by fixed-bed adsorption is necessary. Among the candidate materials for this purpose are activated carbons [23], zeolites [24], metal–organic frameworks [3], graphene oxides [25], greenificated molecularly imprinted polymers [26], etc. To the best of our knowledge, few works have reported breakthrough studies at low temperatures, most of them for H_2/D_2 at 77 K by using a liquid N_2 bath [27–30]. Additionally, most of the adsorption equilibrium data measured for CH_4 and H_2 reported in the literature at low temperatures was obtained by gravimetric or volumetric apparatus that do not allow the study at the same time the dynamics of sorption in single or multicomponent systems (Table S1). The apparatus developed in this work can perform such experiments in a wide range of temperatures (77 to 273 K or above) by simply using different cooling baths either by combining liquid N_2 and dry ice with proper solvents that are stable, reproducible, and cheap to set-up. Moreover, the apparatus that was developed allows also the measurement of adsorption equilibrium and dynamic information for single and also multicomponent interactions that are missing in the literature. Thus, the present work reports the development and validation of a novel fixed-bed adsorption apparatus to carry out adsorption breakthrough curve experiments under cryogenic conditions to screen new adsorbents.

To validate the novel cryogenic fixed-bed adsorption apparatus, breakthrough curve experiments of CH_4 and H_2, and their mixtures on binder-free zeolite 13X were performed. The equilibrium data and the isosteric heat of adsorption measured in this work were compared with the data available in the literature obtained by microcalorimetric, gravimetric, and volumetric methods. Additionally, a mathematical model was implemented on a personal computer to describe the dynamics of the fixed bed adsorption system developed. The data collected and the model is now being used to study the cyclic operation (PSA) for the separation of CH_4/H_2 under cryogenic and high-pressure conditions.

2. Experimental section

2.1. Materials

The binder-free beads of zeolite 13X (13XBFK) were supplied by Chemiewerk Bad Koestritz GmbH (Germany), which consist of spherical particles with a diameter size ranging from 1.6 to 2.5 mm made with 13XBFK crystals with an average diameter of 2 μm. The synthesis and characterization are described in detail elsewhere [31] and the textural properties are summarized in Table S2 in the Supporting Information

(SI).

2.2. Cryogenic fixed-bed apparatus description

The cryogenic fixed-bed adsorption apparatus developed consists of three main sections, namely: (I) gas preparation section, (II) adsorption column, and (III) analytical gas section. A representative schematic of the breakthrough apparatus is shown in Fig. 1.

In the gas preparation section, the partial pressure of the CH_4 and H_2, and their mixtures are set up before being introduced in the adsorption column. Four mass flow controllers (MFC1, 2, 3, and 4 - Bronkhorst High-Tech B.V., the Netherlands) are used to set up the flow rates of inert gas (He), carrier gas (N_2), and adsorbate gases (H_2 and CH_4) at the desired level. Additionally, a back-pressure controller (BPC - Bronkhorst High-Tech B.V., the Netherlands) is used to control the adsorption column pressure at the desired level. Thus, in Fig. 1, the mixture or a pure adsorbate gas enters valve V1 from line 1 and goes out through line 4, by-pass the adsorption column, flows through BPC, and is sent to vent through line 6. Additionally, the carrier gas enters line 4 to drag out faster the molecules that are exiting the column and to keep a constant flow in the system which is important to avoid fluctuation in the back-pressure controller. At the same time, an inert gas enters valve V1 from line 2, goes out through line 3, and runs to the adsorption column to keep it cleaned. The inert gas joins to the adsorbate species and carrier gas before entering the BPC and is sent to the vent from line 6. Helium (MFC3) is cut before starting the experiment and the remaining helium inside the column is displaced by the adsorbates molecules.

In the adsorption section, an adsorption column (stainless steel) dimension of 0.0046 m internal diameter and 0.1 m length is immersed in a Dewar flask cooling bath with a magnetic stirring to keep the temperature homogeneous. The temperature of the cooling bath is determined both by the appropriate use of a solvent (acetone, acetonitrile, and water) as well as a cryogenic agent (dry ice, and ice). Three temperatures are chosen to carry out the experiments that are 195, 231, and 273 K. To set up these temperatures a mixture of acetone/dry ice (195 K), acetonitrile/dry ice (231 K), and water/ice (273 K) is used. These baths are generally reproducible to ± 1 K if they are agitated intermittently and if only a small excess of dry ice is used [32,33]. Additionally, the temperature can be increased up to 333 K by using the water bath with a heater, and also the temperature can be decreased to 77 K by using liquid N_2 baths. The temperature in the cooling bath is controlled with a data-logging refrigerator thermometer (VWR), measuring in a range of 183 to 378 K with an accuracy of ± 0.2 K.

Therefore, after establishing temperature, pressure, and flow rates, the single or multicomponent experiment is started by changing the position of valve V1. Thus, the adsorbate species enter the adsorption column through line 3, flow through the BPC, and go directly to the TCD through line 5 to perform the single component experiment or go to the sample valve V3 through line 6 to perform multi-component experiments. In the case of a multi-component experiment, valve V3 is programmed to change its position at 5 s between load and inject position. In the load position, the sample mixture (CH_4/H_2) enters valve V4, flows through the loop sample (5 μL), and goes out to the vent. In inject position, the carrier gas enters the valve V4 and drags out the sample trapped in the loop that enters the split/splitless (SSL at 423 K) injector to be diluted (1:100) and thereafter enter the capillary column (Molar sieve 5A-plot: length (15 m), ID (0.53 mm), and film thickness (50 μm)) before being analyzed in the TCD (at 423 K). Additionally, from the MFC3 it is possible to input a pure flowrate of He, H_2, or CH_4, useful when it is necessary to start an experiment with the column already saturated with pure H_2 or CH_4.

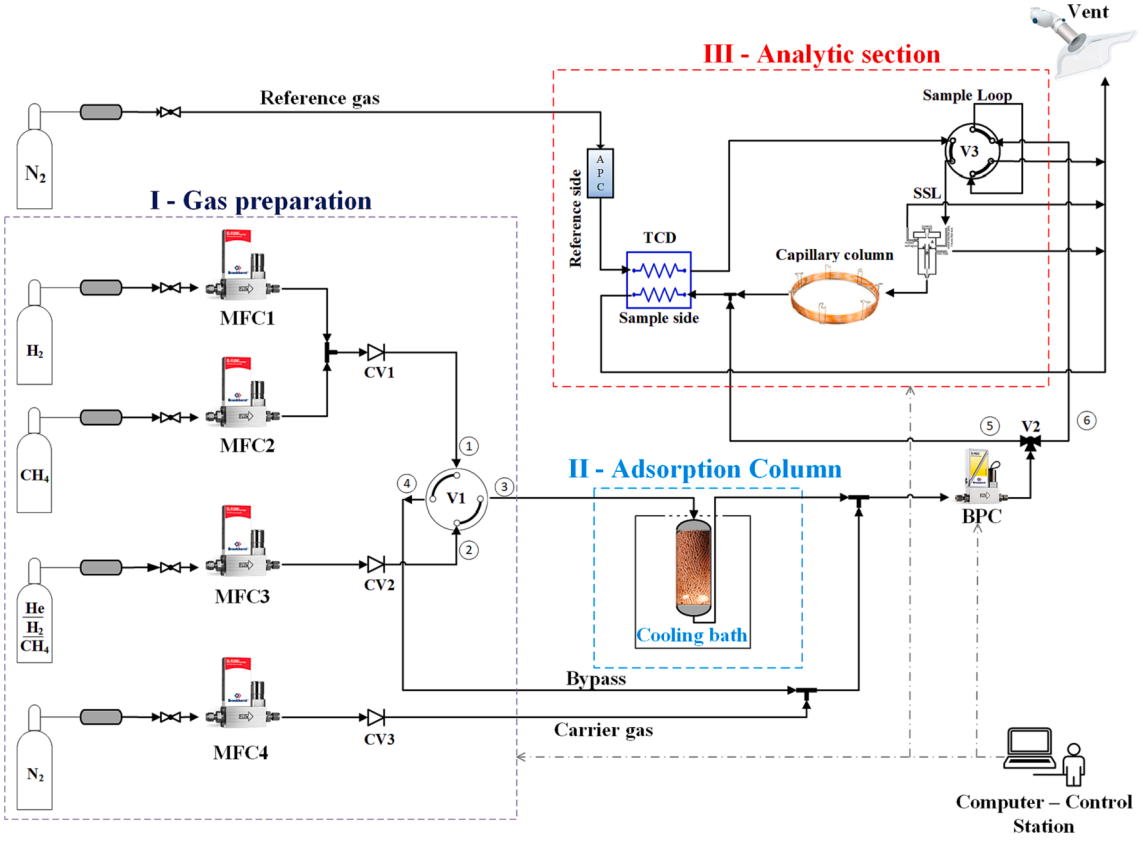

Fig. 1. Schematic diagram of the cryogenic fixed-bed apparatus. MFC mass flow controller; BPC back pressure controller; V1, V2, and V3 valves (V1: 4-way valve, V2: 3-way valve, V3: 6-way valve); CV1, CV2, and CV3 check valves; APC advanced pneumatic control; TCD thermal conductivity detector; Capillary column (Molar sieve 5A-plot).

2.3. Experimental procedure

Before the first run, the adsorption column filled with 13XBFK was activated for 12 h at 623 K under vacuum and pure He flow (10 NmL/min) to remove any pre-adsorbed undesirable components, mainly water, in a Thermconcept Muffle Furnace (Germany), separated from the principal unit. After the activation, the column was sealed (by using VCR® Metal Gasket Face Seal Fitting – Swagelok), weighed to determine the dry adsorbent mass, and finally transferred to the principal apparatus to perform the measurements. Between the runs, the column is heated up to room temperature and cooled back to the experiment temperature under pure He flows (20 NmL/min) to keep the column clean for the next run.

Single component breakthrough experiments of CH_4 and H_2 were performed at three temperatures (195, 231, and 273 K) and pressures up to 18 bar. Tables S3 and S4 summarize the experimental conditions for the single component breakthrough runs of CH_4 and H_2 on a bed, respectively. Additionally, blank runs (column filled with glass sphere) at the same conditions shown in Tables S3 and S4 were performed to consider the system dead volume.

Therefore, after discounting the dead volume, the equilibrium loading is obtained by integrating the molar flow profiles of the breakthrough curves by the following equation,

$$q_{exp,i} = \frac{1}{m_{ads}}\left(F_{fi}t_n - \int_0^{t_\infty} F_i dt - \varepsilon_b V_c C_{0i}\right) \tag{1}$$

where m_{ads} is the adsorbent mass, F_{fi} is the feed molar flow rate of component i at the inlet of the bed, F_i is the molar flow rate of component i at the outlet of the bed, t_∞ is the saturation time, ε_b is the bed porosity, V_c is the column adsorption volume, and C_{0i} is the feed gas-phase concentration at the inlet of the fixed bed.

Binary mixture breakthrough curves were performed considering a mixture of CH_4/H_2 (80/20 vol%) which is the maximum H_2 concentration allowed to be injected into the NG grids. The binary experiments started with a column saturated with H_2. The binary experimental conditions are summarized in Table S5 (in SI).

2.4. Adsorption equilibrium model

To evaluate the CH_4 adsorption equilibrium and isosteric heat on 13XBFK two isotherm models were applied, namely virial and dual-site Langmuir isotherms. For the H_2 adsorption equilibrium and isosteric heat, the standard Langmuir model was applied.

The Virial isotherm is given by [34,35],

$$\ln p = \ln q + \frac{1}{T}\sum_{i=0}^{N1} A_i q^i + \sum_{i=0}^{N2} B_i q^i \tag{2}$$

where p is the pressure in bar, q is the total amount adsorbed in mol kg^{-1}, T is the temperature in K (in this analysis T is 195, 231, and 273 K), A_i and B_i are the virial coefficients, N_1 and N_2 are the number of each virial coefficient required to adequately fit the isotherms.

The virial isotherm is considered to be empirical, however, the parameters A_0 and B_0 are directly connected with quantities having a physical meaning [34], namely

$$\Delta H_0 = -RA_0 \tag{3}$$

$$K_H = K_0 \exp[\Delta H_0/(RT)] \tag{4}$$

$$K_0 = \exp(-B_0) \tag{5}$$

where ΔH_0 is the isosteric heat at zero coverage in kJ mol^{-1}, K_H is Henry's constant in bar kg mol^{-1}, and K_0 the pre-exponential factor in bar kg mol^{-1}.

The isosteric heat of adsorption as a function of coverage can be obtained by combining equation (3) with the Clausius-Clapeyron equation, which leads to

$$\Delta H_{st} = -R\left[\frac{\partial \ln p}{\partial(1/T)}\right] = -R\sum_{i=0}^{N1} A_i q^i \tag{6}$$

The virial fitting of the experimental data was performed by a nonlinear least-square optimization procedure in which the square differences between the experimental and predicted points were weighted according to the error function [34]:

$$\sigma^2 = (1/N)\sum_{i=1}^{n}\left(\ln p_i^{exp} - \ln p_i^{eq.(2)}\right)^2 \tag{7}$$

The dual-site Langmuir (DSL) isotherm is given by,

$$q^* = q_{m1,i}\frac{b_{1i}p_i}{1+b_{1i}p_i} + q_{m2,i}\frac{b_{2i}p_i}{1+b_{2i}p_i} \tag{8}$$

where $q_{m1,i}$ and $q_{m2,i}$ are the maximum adsorbed concentration of component i in each site, b_{1i} and b_{2i} are the adsorption affinity constant of component i in each site.

The effect of temperature on the adsorption affinity constant, b_i is taken into account by the van't Hoff expression,

$$b_i = b_{\infty,i}e^{\left(-\frac{\Delta H_i}{RT}\right)} \tag{9}$$

where $b_{\infty,i}$ is the pre-exponential factor of the affinity constant at infinite temperature, R is the ideal gas constant, $(-\Delta H_i)$ is the heat of adsorption, and T is the temperature.

The dual- and one-site Langmuir fitting of the experimental data was carried out by a nonlinear least-square optimization procedure in which the differences between the experimental and predicted points were weighted according to the error function:

$$\sigma^2 = (1/N)\sum_{i=1}^{n}\left(q_i^{exp} - q_i^{eq.(8)}\right)^2 \tag{10}$$

In the case of DSL model, the isosteric heat of adsorption can be predicted by the differentiation of the DSL model, assuming constant loading ($dq = 0$), and substitute the result in the Clausius-Clapeyron equation, resulting in the following equation [36,37],

$$(-\Delta H_{st}) = \frac{q_{m1}\frac{b_1\Delta H_1}{(1+b_1p)^2} + q_{m2}\frac{b_2\Delta H_2}{(1+b_2p)^2}}{q_{m1}\frac{b_1}{(1+b_1p)^2} + q_{m2}\frac{b_2}{(1+b_2p)^2}} \tag{11}$$

The extended DSL model isotherm, which is sufficiently flexible to provide a suitable mathematical form to predict gas isotherms [21], was used to predict the interaction of binary mixture CH_4/H_2 systems by the following equation,

$$q_i^* = q_{m1,i}\frac{b_{1i}p_i}{1+\sum_{j=1}^{n} b_{1j}p_j} + q_{m2,i}\frac{b_{2i}p_i}{1+\sum_{j=1}^{n} b_{2j}p_j} \tag{12}$$

2.5. Mathematical modeling

The dynamic behavior of adsorption processes can be numerically predicted according to the mass and energy conservation laws. The mathematical model employed for the simulation of the breakthrough curves in this work includes both the effect of axial dispersion and mass transfer resistances. The sorbate adsorption kinetics is taken into account by the linear rate driving force model (LDF) [38–40]. The set of coupled partial and algebraic differential equations that represent the fixed bed adsorption model are summarized in Table 1 and the respective initial and boundary conditions are summarized in Table S6 in SI.

For the solution of the model, the set of coupled partial and algebraic differential equations is reduced into a system of ordinary and algebraic differential equations by the method of the lines [41]. Orthogonal

Table 1
Adsorption mathematical model.

Phenomenon model	Equations	
ideal gas	$C = \frac{P}{RT}$	(13)
overall mass balance	$\frac{\partial F}{\partial z} + \varepsilon_b \frac{\partial C}{\partial t} + \rho_p(1-\varepsilon_b)\sum_{i=1}^{n}\frac{\partial \overline{q}_i}{\partial t} = 0$	(14)
component mass balance	$-\varepsilon_b D_{ax}\frac{\partial}{\partial z}\left(C\frac{\partial y_i}{\partial z}\right) + \frac{\partial (Fy_i)}{\partial z} + \varepsilon_b \frac{\partial (Cy_i)}{\partial t} + \rho_p(1-\varepsilon_b)\frac{\partial \overline{q}_i}{\partial t} = 0$	(15)
mass transfer rate	$\frac{\partial \overline{q}_i}{\partial t} = K_{LDF}(q^* - \overline{q}_i)$	(16)
gas-phase energy balance	$-K_{ax}\frac{\partial^2 T}{\partial z^2} + Fc_{pg}\frac{\partial T}{\partial z} + C\varepsilon_b C_{pg}\frac{\partial T}{\partial t} + (1-\varepsilon_b)a_p h_p(T-T_s) + a_c h_w(T-T_w) = 0$	(17)
solid-phase energy balance	$C_{ps}\frac{\partial T_s}{\partial t} = a_p h_p(T-T_s) + \rho_p \sum_{i=1}^{n}(-\Delta H_{st,i})\frac{\partial \overline{q}_i}{\partial t}$	(18)
isotherm model (DSL)	$q_i^* = \frac{q_{m1} b_{1i} p_i}{1+\sum_{j=1}^{n} b_{1j} p_j} + \frac{q_{m2} b_{2i} p_i}{1+\sum_{j=1}^{n} b_{2j} p_j}$	(12)

Collocation method was applied to discretize the spatial coordinate [42]. The computation of the collocation points was determined by the position on the spatial coordinate using Jacobi polynomial, $P_{N^{(\alpha,\beta)}}(x)$, with $\alpha = 0$ and $\beta = 0$. The approximation of the first and second derivatives was made by collocation matrices routines $A_{i,j}$ and $B_{i,j}$, respectively. Thus, the system of ordinary differential equations has been solved using ode15s, a stiff ODE solver available in the MATLAB library [43], and the algebraic differential equations were solved by Gauss elimination. Twenty-five special collocation points appeared to give satisfactory accuracy and stability to the numerical solution. The solution has been implemented on a personal computer.

3. Results and discussion

3.1. Adsorption equilibrium

To set up the adsorption isotherms of CH_4 and H_2 in the binder-free zeolite 13X a series of breakthrough curves were measured at three temperatures, 195, 231, and 273 K, and pressures up to 18 bar. The experimental conditions are summarized in Tables S3 and S4 in the SI. Fig. 2a-b shows the observed experimental breakthrough curves at 195 K plotted in terms of normalized molar fraction y_i/y_{i0} against moles fed per unit mass of adsorbent (13XBFK), for (a) CH_4, and (b) H_2. The breakthrough curves observed for CH_4 and H_2 on 13XBFK at 231 and 273 K are shown in Figs. S2 and S3 of the SI. It is clear from Fig. 2a that the moles fed to reach the breakthrough of CH_4 are much higher than in the case of H_2 (Fig. 2b). Moreover, as the pressure increases (from Run me11 to me15, and Run hy11 to hy15) the moles fed to reach breakthrough increases which indicate that the data are thermodynamically consistent, according to a type I isotherm. In other words, as higher the pressure of sorption higher the amount adsorbed into the material.

Fig. 3. shows the experimental (symbols) and theoretical (lines) isotherms measured for (a) CH_4 and (b) H_2 on 13XBFK. As can be seen, the amount adsorbed of CH_4 and H_2 increases by enhancing the partial pressure and decreases by increasing the temperature. At 195 K and 12 bar, the equilibrium loading for CH_4 and H_2 is 6.94 and 2.08 mol/kg (Runs me15 and hy15). From Fig. 3 we can see that both isotherms are type I (favorable for adsorption), being the CH_4 isotherm shape steeper than H_2 at low loadings due to its higher affinity with the 13XBFK framework.

Table 2 shows the virial, dual-site, and standard Langmuir isotherms parameters calculated from the fitting of the adsorption equilibrium data for CH_4 and H_2 shown in Fig. 3. The lines in Fig. 3a show that the DSL and virial isotherm models describe conveniently the CH_4 equilibrium data. To fit the CH_4 adsorption equilibrium data into equation (2), it was considered the number of virial coefficients N_1 equal to 5, and N_2 equal to 2. In this way, equation (2) has five virial coefficients A and two coefficients B shown in Table 2.

The H_2 adsorption isotherm is almost linear in 13XBFK as can be seen in Fig. 3b. For this set of data, different combinations of isotherm model parameters provide a good fit. To avoid a combination of parameters that do not have a physical meaning, it was used the maximum loading observed in the literature for H_2 adsorption in NaX in the fitting procedure. Du and Wu [44] have studied the physisorption of H_2 in A, X, and ZSM-5 types of zeolites at moderately high pressures and cryogenic temperatures. At 40 bar and 77 K, they observed a maximum loading for H_2 in NaX around 12.65 mol kg^{-1}. This maximum loading was used as the boundary to fit the Langmuir isotherm in this work, which provides a great fit and description of H_2 data as we can see in Fig. 3b. It is worth mentioning that the set of parameters for both H_2 and CH_4 isotherms must be used only in the range of conditions studied in this work.

We compare the CH_4 loading obtained in conventional zeolite 13X pellets made by an inert binder (c.a. 15–25 %) with binder-free zeolite 13X beads studied in this work. At 195 K and 1 bar, the CH_4 loading in a conventional zeolite 13X is approximately 4.20 mol kg^{-1} [45], while the loading obtained in this work was 5.20 mol kg^{-1}. This difference (20 %) is exactly the amount of inert binder present in the conventional zeolite 13X that decreases its adsorption capacity. In the case of the binder-free method, the binder is itself transformed into zeolite matter during the hydrothermal conversion [46], increasing the adsorption capacity of the final zeolite beads. This result points out an opportunity to decrease the

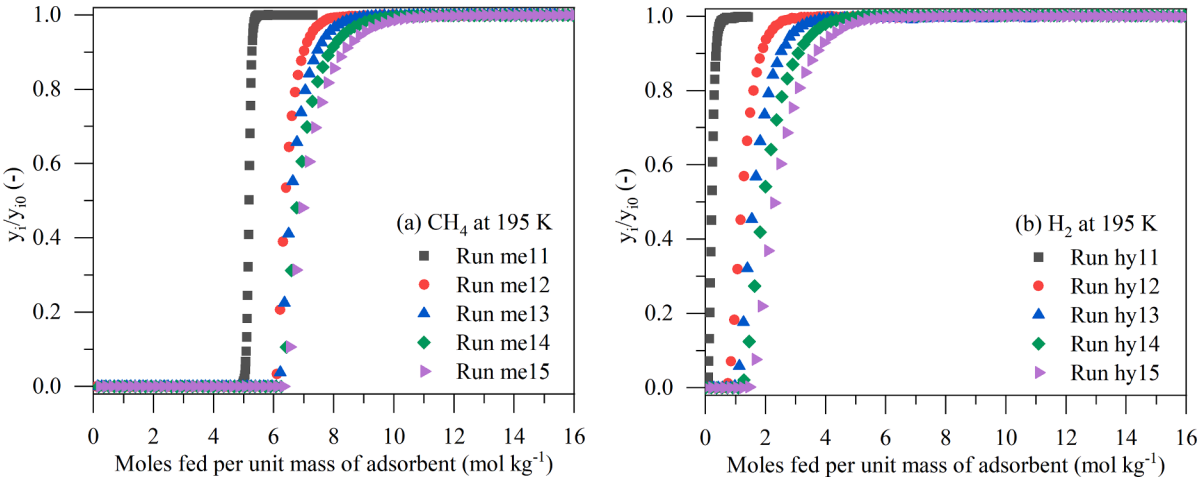

Fig. 2. Experimental breakthrough curves of (a) CH_4 and (b) H_2 on binder-free zeolite 13X at 195 K. The experimental conditions of each run (Run meX for methane and Run hyX for hydrogen) can be found in Tables S3 and S4.

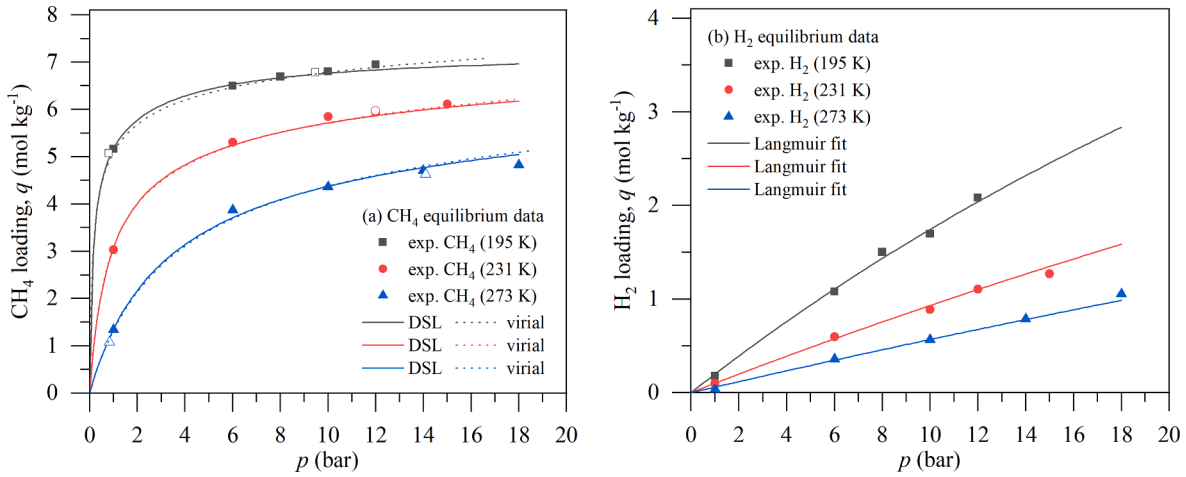

Fig. 3. Adsorption equilibrium of (a) CH_4 and (b) H_2 on binder-free zeolite 13X. Symbols = experimental; Solid lines = model. Open symbols for CH_4 represent its loading in a mixture with H_2.

Table 2
Langmuir and Virial isotherm model parameters for sorption of CH_4 and H_2 on binder-free zeolite 13X.

dual-site and standard Langmuir isotherm model

Species	q_m(mol kg^{-1})		b(bar^{-1})[a]		(ΔH_i)(kJ mol^{-1})			σ^2
	q_{m1}	q_{m2}	b_1	b_2	$(\Delta H_i)_1$	$(\Delta H_i)_2$		
CH_4	2.13	5.12	0.41	8.04	−16.1	−18.0		0.008
H_2	12.65	–	0.016	–	−7.0	–		0.002

virial isotherm model

Specie	A_i(kg mol^{-1}K)					B_i(kg mol^{-1})		
CH_4	A_0	A_1	A_2	A_3	A_4	B_0	B_1	σ^2
	−2285.3	21.7	0.10	1.07	0.08	7.79	0.14	0.009

[a] The reference temperature used is 195 K.

size of an adsorption column by 20 % which reduces the CAPEX and OPEX in the industrial process. Additionally, to verify whether the equilibrium data obtained in this new experimental unit is reliable or not, we compare the CH_4 loading on the crystal of zeolite 13X and in a binder-free zeolite 13X. The comparison is shown in Figure S4 (in SI) where it is shown quite similar results.

3.2. Isosteric heat of adsorption

According to the virial isotherm, semilog plots of p/q vs q extrapolated to zero concentration give us Henry's constants (equation (4)), which are useful to check the thermodynamic consistency of experimental data. Fig. 4 shows semilog plots of p/q vs q for the CH_4 isotherms.

By extrapolation until zero coverage, it is possible to obtain Henry's constants for each curve [47], which leads to 0.566, 0.135, and 0.020 bar kg mol^{-1} at 273, 231, and 195 K, respectively. Manipulating the equation (4) and substituting two Henry's constants, for example, Henry's constants at 195 and 273 K, we can evaluate the heat of adsorption at a zero coverage ($-\Delta H_{st}|_{q=0}$), which is 19.0 kJ mol^{-1}. Table 3 summarizes the isosteric heat of adsorption at the limit of zero loading reported in the literature. It is possible to see that the value of isosteric heat of adsorption obtained in this work is within the range of the values reported in Table 3.

Additionally, from the dual-site Langmuir fitting, the heat of adsorption was predicted to be around −16.1 and −18.0 kJ mol^{-1} (see Table 2) which is very close to the one predicted by the virial analysis. From virial analysis, we conclude that the CH_4 equilibrium data on 13XBFK obtained in this work is thermodynamic consistent. Although

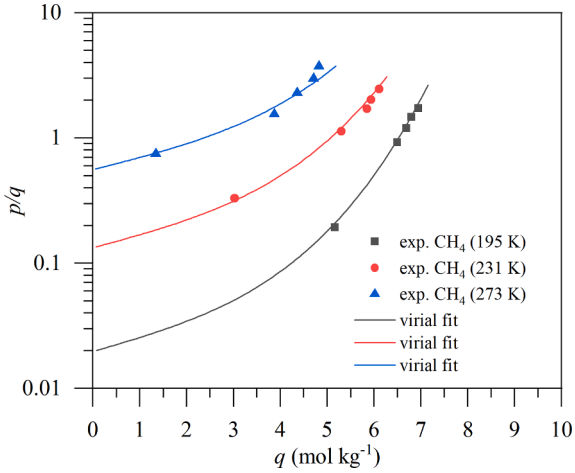

Fig. 4. The virial semilog plots of p/q vs q for the CH_4 isotherm.

we do not have equilibrium data in low-pressure regions, the extrapolation of virial isotherm to the limit of zero loading allows us to obtain consistent values of Henry's constants, which fits well with the literature.

Furthermore, the behavior of isosteric heat of adsorption as a function of coverage was predicted by applying equations (6) (from virial isotherm) and 11 (from dual-site Langmuir isotherm). Fig. 5 shows the isosteric heat of adsorption as a function of coverage for CH_4 on 13XBFK

Table 3
Isosteric heat of adsorption at the limit of zero loading, $-\Delta H_{st}|_{q=0}$, for the adsorption of CH_4 in zeolite 13X.

Reference	$-\Delta H_{st}\|_{q=0}$(kJ/mol)
Barrer and Sutherland (1956) [48]	18.8
Habgood (1964) [49]	17.6
Zhang *et al.* (1991) [50]	20.1
Cavenati *et al.* (2004) [51]	15.3
Maurin et al. (2006) [52]	19.1
Llano-Restrepo (2010) [53]	19.2
Moreira *et al.* (2017) [54]	25.7
This work	19.0

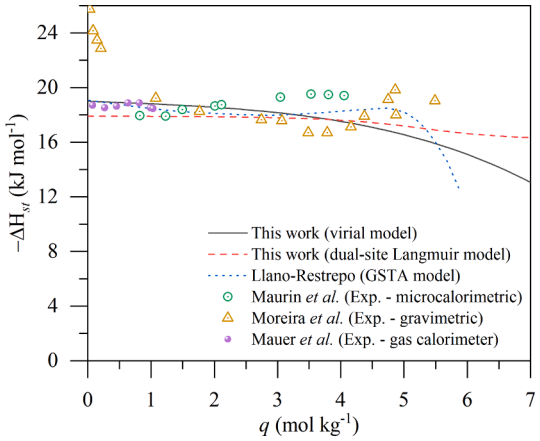

Fig. 5. Isosteric heat of adsorption as a function of coverage for CH_4 on 13XBFK.

and a comparison with data available in the literature. It can be seen that the overall behavior of the isosteric heat is similar to the ones predicted by Llno-Restrepo [53], Maurin *et al.* [52], Moreira *et al.* [54], and Mauer *et al.* [55].

In the case of H_2, the isosteric heat of adsorption predicted by the standard Langmuir model is constant at around −7.0 kJ mol^{-1} (see Table 2), since the Langmuir model considers that all active sites are energetically equal, and thus, the isosteric heat of adsorption will be constant as a function of coverage. This value is within the range reported in the literature [44,56,57], which points out that the data obtained in this new cryogenic fixed-bed adsorption is consistent.

It is worth mentioning that the values of equilibrium and isosteric heat for both CH_4 and H_2 obtained by the breakthrough curves technique agree very well with the ones reported in the literature that were obtained through gravimetric, calorimetric, and volumetric techniques [44,52–57]. Additionally, the analysis of isosteric heat of adsorption pointed out that the data obtained from the novel apparatus is thermodynamic consistent, reliable, and agrees with the literature.

3.3. Binary adsorption and simulation

For the binary separation studies, it was considered a mixture ratio of CH_4/H_2 equal to 80/20 vol%. This amount of H_2 blended with CH_4 is close to the range allowed 4–10 % (v/v) in Austria and Germany [21], respectively. Additionally, it is close to Portugal's target of injecting 15 vol% of H_2 into NG pipelines by 2030 [58]. The adsorption column, in this set of binary experiments, started saturated with pure H_2 at the experimental condition shown in Table S5.

Fig. 6 shows the binary breakthrough curves of CH_4/H_2 on 13XBFK at (a) 273, (b) 231, and (c) 195 K. As can be seen, the breakthrough time increases as the temperature decreases, for example, at 273 K the breakthrough time is around 5.6 min against 9.2 min at 195 K. This effect is expected since the CH_4 sorption into 13XBFK is strongly dependent on temperature as shown in Fig. 1. From each binary breakthrough curve, it was possible to calculate the CH_4 amount adsorbed that was compared with the ones obtained in the single CH_4 breakthrough curves. The CH_4 loadings in a mixture with H_2 are shown in Fig. 1 represented by the open symbols. As can be seen, the CH_4 loadings in a mixture with H_2 are very close to the ones observed in a single component system, which means that H_2 practically doesn't compete with CH_4 for sorption in 13XBFK at the studied operating conditions. This observation can also be checked through the calculated selectivity of 17.3, $\left(q^*_{CH4}/y_{CH4}\right)/\left(q^*_{H2}/y_{H2}\right)$, predicted by the extended DSL model (eq. (12)) for a mixture of CH_4(80 %)/H_2(20 %) at 195 K and 12 bar. Both CH_4 and H_2 can enter 13X frameworks easily without a pore-blocking effect as their kinetic diameters (3.80 and 2.89 Å, respectively [56]) are lower than the free diameter of the aperture (9.00 Å [44]) [44,52,59]. It is well known that the cations inside the frameworks interact with polar and easily polarizable molecules [60]. In this way, a possible explanation for the higher interaction of CH_4 instead of H_2 may be their polarizability difference. The polarizability of CH_4 is 2.45 Å^3 whereas that of H_2 is 0.79 Å^3 [56]. Thus, when CH_4 and H_2 are subjected to the electric field inside the framework both acquire an electric dipole moment proportional to the electric field. As CH_4 has a bigger polarizability, it will interact stronger with the framework as compared with H_2.

To perform the simulation of the binary breakthrough curves, the transport parameters, namely axial dispersion (D_{ax}), effective axial bed thermal conductivity (K_{ax}), film heat transfer (h_p), and the heat capacity of gas (C_{pg}) were obtained by commonly used correlations summarized in Table S7. The mass transfer of CH_4 and H_2 on zeolite 13X has already known in the literature, thus, the inputted values of mass transfer are taken elsewhere [54,61]. Streb *et al.* [61] have assumed a high mass transfer of H_2 on zeolite 13X equal to 1.0 s^{-1} and have justified that the mass transfer of H_2 is known to be very fast on zeolite 13X. Moreira *et al.* [54] have reported a homogeneous mass transfer coefficient for CH_4 on zeolite 13X represented by $k_h = 2.7 \times 10^{-4} e^{1.4\times10^{-2}T}$. In the simulations, to achieve the best fit, it was necessary to adjust the mass transfer for CH_4 up to 60 % higher than that predicted by the previous equation.

The parameter values used in the simulation are summarized in Table 4. The lines in Fig. 6 represent the simulation results which agree very well with the experimental data. Additionally, as the set of conditions that we have studied are near the critical conditions, it was evaluated if the ideal gas law is still valid to describe the experiments. In this view, it was set up the mathematical model in the Aspen Adsorption simulator and repeated the simulations by comparing the two equations of state: i) Ideal Gas Law and ii) Peng-Robinson. The Aspen simulation results are shown in the SI (Fig. S1). Briefly, the results clearly show that both equations of state give similar results. Thus, although the temperature and pressure are near the critical conditions for CH_4, the ideal gas law still gives a good prediction of the fixed bed adsorption.

4. Conclusions

In this work, a novel fixed-bed adsorption apparatus was developed and validated to carry out adsorption breakthrough curve experiments at cryogenic temperatures (195–273 K) and high pressures (up to 18 bar) to screen candidate adsorbents for dynamic separation of H_2 from natural gas grids. The benchmark binder-free zeolite 13X was chosen to validate the apparatus by performing breakthrough curve experiments of CH_4 and H_2, and their mixtures. The viral and dual-site Langmuir isotherm model fits conveniently the CH_4 equilibrium, and the standard Langmuir isotherm model provides a good description of the H_2 equilibrium data on binder-free zeolite 13X. Both isotherms are type I being CH_4 more adsorbed than H_2 due to its higher polarizability. Furthermore, the CH_4 and H_2 isosteric heat of adsorption agree with data available in the literature obtained by microcalorimetric, gravimetric, and volumetric methods. This comparison pointed out that the

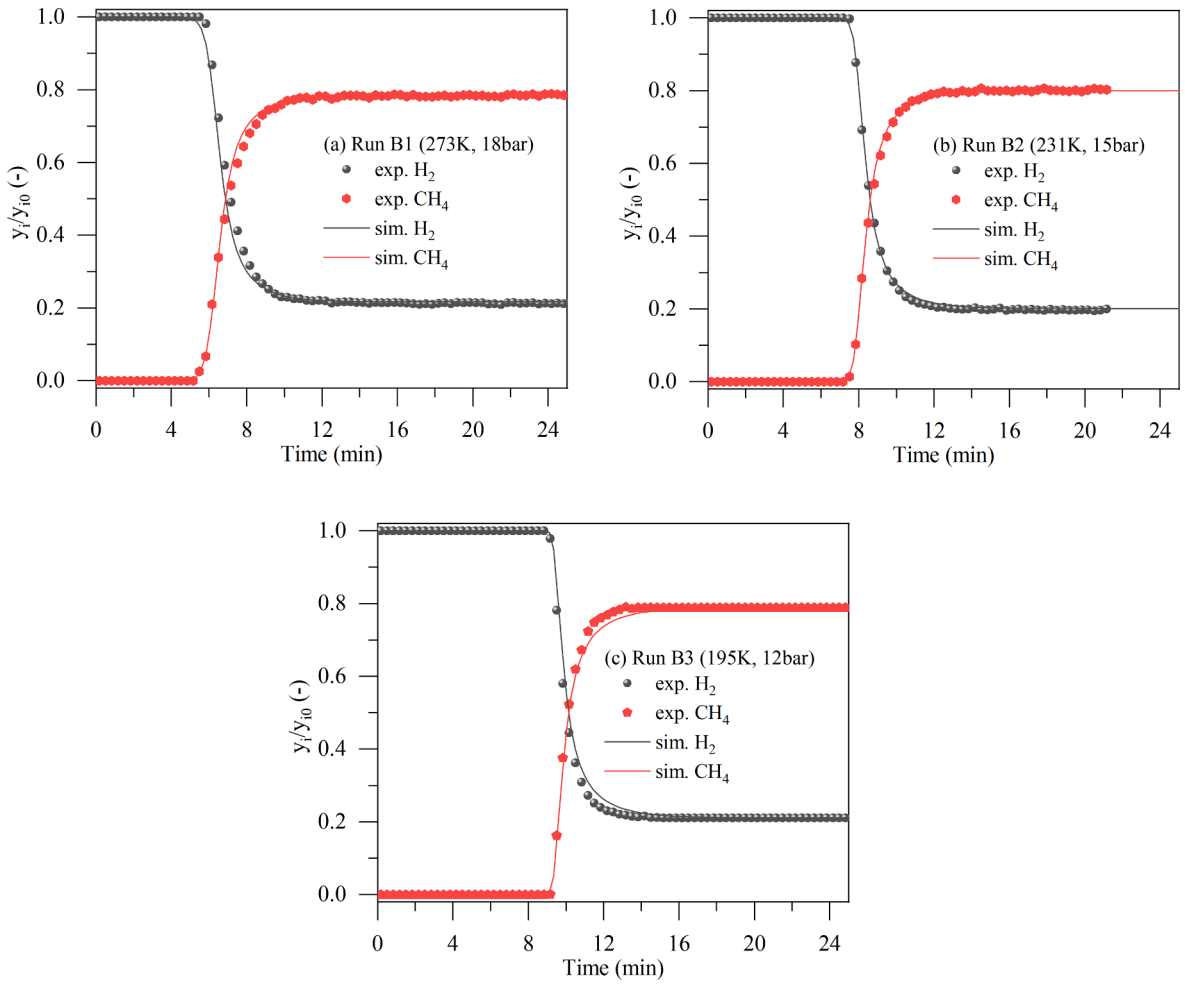

Fig. 6. Adsorption breakthrough curves for a mixture ratio CH_4/H_2 (80/20 vol%) on binder-free zeolite 13X at (a) 273, (b) 231, and (c) 195 K.

Table 4
Parameters values for the simulations.

Run	$K_{LDF,H2}$ (s^{-1})	$K_{LDF,CH4}$ (s^{-1})	D_{ax} ($m^2\ s^{-1}$)	K_{ax} ($Wm^{-1}\ K^{-1}$)	C_{pg} ($Jmol\ K^{-1}$)	h_p ($Wm^{-2}\ K^{-1}$)	h_w ($Wm^{-2}\ K^{-1}$)
B1	1.00	1.30×10^{-2}	4.08×10^{-6}	1.00	33.5	116.8	40.0
B2	1.00	1.15×10^{-2}	3.11×10^{-6}	0.95	32.6	99.8	40.0
B3	1.00	1.02×10^{-2}	3.67×10^{-6}	0.92	31.9	88.3	40.0

equilibrium data obtained in the new cryogenic apparatus are thermodynamic consistent. Additionally, binary experiments were performed to evaluate the dynamic separation of H_2 and CH_4 at the ratio H_2/CH_4 (20/80 % vol.) and also simulated by using a dynamic fixed-bed mathematical model that considers linear driving force model and axial dispersion. To perform the simulations, the extended dual-site Langmuir model was used and it provided a good prediction of the competitive interaction between species. Overall, the results pointed out that the novel apparatus provides reliable means to collect equilibrium and dynamic information under cryogenic conditions for screening candidates targeting the separation of H_2 from natural gas.

CRediT authorship contribution statement

Lucas F.A.S. Zafanelli: Investigation, Formal analysis, Software, Conceptualization, Methodology, Validation, Writing – original draft. **Ezzeldin Aly:** Investigation, Validation, Writing – review & editing. **Alírio E. Rodrigues:** Supervision, Visualization, Validation, Funding acquisition, Project administration, Writing – review & editing. **José A. C. Silva:** Supervision, Visualization, Validation, Funding acquisition, Project administration, Resources, Writing – review & editing.

Declaration of Competing Interest

The authors declare that they have no known competing financial interests or personal relationships that could have appeared to influence the work reported in this paper.

Data availability

Data will be made available on request.

Acknowledgments

The authors are grateful to the Foundation for Science and Technology (FCT, Portugal) under project PTDC 2020 * 3599-PPCDTI * Engenharia dos Processos Químicos * project PTDC/EQU- EPQ/0467/2020. Also, through national funds FCT/MCTES (PIDDAC) to CIMO

(UIDB/00690/2020 and UIDP/00690/2020), SusTEC (LA/P/0007/2021), ALiCE (LA/P/0045/2020), and LSRE-LCM (UIDB/50020/2020 and UIDP/50020/2020). Additionally, we thank national funding by FCT, Foundation for Science and Technology, through the individual research grant SFRH/BD/7925/2020 of Lucas F. A. S. Zafanelli. Moreover, the authors are grateful to Kristin Gleichmann and Chemiewerk Bad Koestritz GmbH for kindly providing the binder-free beads of zeolite 13X studied in this work.

Appendix A. Supplementary material

Supplementary data to this article can be found online at https://doi.org/10.1016/j.seppur.2022.122824.

References

[1] M. Cavana, P. Leone, Solar hydrogen from North Africa to Europe through greenstream: a simulation-based analysis of blending scenarios and production plant sizing, Int. J. Hydrogen Energy. 46 (2021) 22618–22637, https://doi.org/10.1016/j.ijhydene.2021.04.065.
[2] S. Atilhan, S. Park, M.M. El-Halwagi, M. Atilhan, M. Moore, R.B. Nielsen, Green hydrogen as an alternative fuel for the shipping industry, Curr. Opin. Chem. Eng. 31 (2021), 100668, https://doi.org/10.1016/j.coche.2020.100668.
[3] A. Schoedel, Z. Ji, O.M. Yaghi, The role of metal–organic frameworks in a carbon-neutral energy cycle, Nat. Energy. 1 (2016) 16034, https://doi.org/10.1038/nenergy.2016.34.
[4] S. van Renssen, The hydrogen solution? Nat. Clim. Chang. 10 (2020) 799–801, https://doi.org/10.1038/s41558-020-0891-0.
[5] H. Council, M. and Co, Hydrogen Insights: A perspective on hydrogen investment, market development and cost competitiveness, 2021. https://hydrogencouncil.com/en/hydrogen-insights-2021/.
[6] J.O. Abe, A.P.I. Popoola, E. Ajenifuja, O.M. Popoola, Hydrogen energy, economy and storage: review and recommendation, Int. J. Hydrogen Energy. 44 (2019) 15072–15086, https://doi.org/10.1016/j.ijhydene.2019.04.068.
[7] R.J. Kuppler, D.J. Timmons, Q.-R. Fang, J.-R. Li, T.A. Makal, M.D. Young, D. Yuan, D. Zhao, W. Zhuang, H.-C. Zhou, Potential applications of metal-organic frameworks, Coord. Chem. Rev. 253 (2009) 3042–3066, https://doi.org/10.1016/j.ccr.2009.05.019.
[8] W.C. Nadaleti, V.A. Lourenço, G. Americo, Green hydrogen-based pathways and alternatives: towards the renewable energy transition in South America's regions – Part A, Int. J. Hydrogen Energy. 46 (2021) 22247–22255, https://doi.org/10.1016/j.ijhydene.2021.03.239.
[9] IRENA, Hydrogen: a renewable energy perspective, 2nd ed., International Renewable Energy Agency, Abu Dhabi, Tokyo, 2019. www.irena.org.
[10] A. van Wijk, The Green Hydrogen Economy in the Northern Netherlands, A report by Noordelijke Innovation Board, Groningen, the Netherlands, 2017. http://verslag.noordelijkeinnovationboard.nl/uploads/bestanden/dbf7757e-cabc-5dd6-9e97-16165b653dad/3008272975/NIB-Hydrogen-Full_report.pdf.
[11] M.W. Melaina, O. Antonia, M. Penev, Blending Hydrogen into Natural Gas Pipeline Networks: A Review of Key Issues, Golden, CO (United States), 2013. https://doi.org/10.2172/1068610.
[12] W. Liemberger, M. Groß, M. Miltner, H. Prazak-Reisinger, M. Harasek, Extraction of green hydrogen at fuel cell quality from mixtures with natural gas, Chem. Eng. Trans. 52 (2016) 427–432, https://doi.org/10.3303/CET1652072.
[13] J.A. Ritter, A.D. Ebner, State-of-the-art adsorption and membrane separation processes for hydrogen production in the chemical and petrochemical industries, Sep. Sci. Technol. 42 (2007) 1123–1193, https://doi.org/10.1080/01496390701242194.
[14] A.M. Ribeiro, C.A. Grande, F.V.S. Lopes, J.M. Loureiro, A.E. Rodrigues, Four beds pressure swing adsorption for hydrogen purification: Case of humid feed and activated carbon beds, AIChE J. 55 (2009) 2292–2302, https://doi.org/10.1002/aic.11886.
[15] A.M. Ribeiro, C.A. Grande, F.V.S. Lopes, J.M. Loureiro, A.E. Rodrigues, A parametric study of layered bed PSA for hydrogen purification, Chem. Eng. Sci. 63 (2008) 5258–5273, https://doi.org/10.1016/j.ces.2008.07.017.
[16] B. Verougstraete, M. Schoukens, B. Sutens, N. Vanden Haute, Y. De Vos, M. Rombouts, J.F.M. Denayer, Electrical swing adsorption on 3D-printed activated carbon monoliths for CO_2 capture from biogas, Sep. Purif. Technol. 299 (2022), 121660, https://doi.org/10.1016/j.seppur.2022.121660.
[17] A. Zapata Ballesteros, N. De Witte, J.F.M. Denayer, T.R.C. Van Assche, Effect of pellet size on PSA performance: monolayer and multilayer bed case study for biogas upgrading, Adsorption. (2022). https://doi.org/10.1007/s10450-022-00365-9.
[18] R.M. Siqueira, G.R. Freitas, H.R. Peixoto, J.F. do Nascimento, A.P.S. Musse, A.E.B. Torres, D.C.S. Azevedo, M. Bastos-Neto, Carbon Dioxide Capture by Pressure Swing Adsorption, Energy Procedia. 114 (2017) 2182–2192. https://doi.org/10.1016/j.egypro.2017.03.1355.
[19] R. Morales-Ospino, R.G. Santiago, R.M. Siqueira, D.C.S. de Azevedo, M. Bastos-Neto, Assessment of CO_2 desorption from 13X zeolite for a prospective TSA process, Adsorption. (2019), https://doi.org/10.1007/s10450-019-00192-5.
[20] Y. Gomez-Rueda, B. Verougstraete, C. Ranga, E. Perez-Botella, F. Reniers, J.F.M. Denayer, Rapid temperature swing adsorption using microwave regeneration for carbon capture, Chem. Eng. J. 446 (2022), 137345, https://doi.org/10.1016/j.cej.2022.137345.
[21] L. Dehdari, I. Burgers, P. Xiao, K. Gang Li, R. Singh, P.A. Webley, Purification of hydrogen from natural gas/hydrogen pipeline mixtures, Sep. Purif. Technol. (2021), 120094, https://doi.org/10.1016/j.seppur.2021.120094.
[22] D. Grainger, M.B. Hägg, The recovery by carbon molecular sieve membranes of hydrogen transmitted in natural gas networks, Int. J. Hydrogen Energy. 33 (2008) 2379–2388, https://doi.org/10.1016/j.ijhydene.2008.03.001.
[23] L.A.M. Rocha, K.A. Andreassen, C.A. Grande, Separation of CO_2 /CH_4 using carbon molecular sieve (CMS) at low and high pressure, Chem. Eng. Sci. 164 (2017) 148–157, https://doi.org/10.1016/j.ces.2017.01.071.
[24] Z. Cao, N.D. Anjikar, S. Yang, Small-pore zeolite membranes: a review of gas separation applications and membrane preparation, Separations. 9 (2022) 47, https://doi.org/10.3390/separations9020047.
[25] L. Wang, K. Lee, Y.-Y. Sun, M. Lucking, Z. Chen, J.J. Zhao, S.B. Zhang, Graphene oxide as an ideal substrate for hydrogen storage, ACS Nano. 3 (2009) 2995–3000, https://doi.org/10.1021/nn900667s.
[26] A. Ostovan, M. Arabi, Y. Wang, J. Li, B. Li, X. Wang, L. Chen, Greenificated molecularly imprinted materials for advanced applications, Adv. Mater. 34 (2022) 2203154, https://doi.org/10.1002/adma.202203154.
[27] K. Munakata, Y. Kawamura, Adsorption behavior of hydrogen and deuterium on natural mordenite adsorbent at 77 K, Fusion Sci. Technol. 62 (2012) 71–76, https://doi.org/10.13182/FST12-A14115.
[28] K. Kotoh, S. Moriyama, S. Takashima, K. Takahashi, Breakthrough curves of non-trace H2–D2 mixture replacement adsorption with SZ-13X packed column at 77.4K, Fusion Eng. Des. 88 (2013) 2223–2227, https://doi.org/10.1016/j.fusengdes.2013.05.074.
[29] K. Kotoh, M. Tanaka, T. Sakamoto, S. Takashima, T. Asakura, T. Uda, T. Sugiyama, Multi-component behavior of hydrogen isotopes in zeolite packed-beds used for cryogenic pressure swing adsorption, Fusion Sci. Technol. 56 (2009) 184–189, https://doi.org/10.13182/FST09-A8899.
[30] S. Kim, H. Oh, Investigation of cryogenic breakthrough curve measurement system at 77 K for hydrogen isotopologue separation, Korean, J. Mater. Res. 32 (2022) 36–43, https://doi.org/10.3740/MRSK.2022.32.1.36.
[31] K. Schumann, A. Brandt, B. Unger, F. Scheffler, Bindemittelfreie zeolithische Molekularsiebe der Typen LTA und FAU, Chemie-Ingenieur-Technik. 83 (2011) 2237–2243, https://doi.org/10.1002/cite.201100151.
[32] A.M. Phipps, D.N. Hume, General purpose low temperature dry-ice baths, J. Chem. Educ. 45 (1968) 664, https://doi.org/10.1021/ed045p664.
[33] L. Riekert, Rates of sorption and diffusion of hydrocarbons in zeolites, AIChE J. 17 (1971) 446–454, https://doi.org/10.1002/aic.690170237.
[34] L. Czepirski, J. JagieŁŁo, Virial-type thermal equation of gas—solid adsorption, Chem. Eng. Sci. 44 (1989) 797–801, https://doi.org/10.1016/0009-2509(89)85253-4.
[35] A. Nuhnen, C. Janiak, A practical guide to calculate the isosteric heat/enthalpy of adsorption: Via adsorption isotherms in metal-organic frameworks, MOFs, Dalt. Trans. 49 (2020) 10295–10307, https://doi.org/10.1039/d0dt01784a.
[36] P.S. Bárcia, M.P.M. Nicolau, J.M. Gallegos, B. Chen, A.E. Rodrigues, J.A.C. Silva, Modeling adsorption equilibria of xylene isomers in a microporous metal-organic framework, Microporous Mesoporous Mater. 155 (2012) 220–226, https://doi.org/10.1016/j.micromeso.2012.01.033.
[37] D.D. Do, Adsorption analysis: equilibria and kinetics, Imperial College Press (1998), https://doi.org/10.1142/9781860943829.
[38] D.M. Ruthven, Principles of Adsorption and Adsorption Processes, 1st ed., John Wiley & Sons, New York, 1984.
[39] E. Glueckauf, Theory of chromatography, J. Chromatogr. Libr. 51 (1955) A1–A68, https://doi.org/10.1016/S0301-4770(08)61562-6.
[40] S. Sircar, J.R. Hufton, A. Products, Why Does the Linear Driving Force Model for, Adsorption Kinetics Work ?, 2000, pp. 137–147.
[41] W.E. Schiesser, G.W. Griffiths, A Compendium of Partial Differential Equation Models, Cambridge University Press, Cambridge, 2009. https://doi.org/10.1017/CBO9780511576270.
[42] J. Villadsen, L.M. Michael, Solution of differential equation models by polynomial approximation, New Jersey, 1978.
[43] L.F. Shampine, M.W. Reichelt, The MATLAB ODE Suite, SIAM J. Sci. Comput. 18 (1997) 1–22.
[44] X. Du, E. Wu, Physisorption of Hydrogen in A, X and ZSM-5 Types of Zeolites at Moderately High Pressures, Chinese, J. Chem. Phys. 19 (2006) 457–462, https://doi.org/10.1360/cjcp2006.19(5).457.6.
[45] C.A. Grande, R. Blom, Cryogenic adsorption of methane and carbon dioxide on zeolites 4A and 13X, Energy & Fuels. 28 (2014) 6688–6693, https://doi.org/10.1021/ef501814x.
[46] K. Gleichmann, B. Unger, A. Brandt, Industrial zeolite molecular sieves, Intech, in, 2016, p. 13.
[47] J.A.C. Silva, A.E. Rodrigues, Sorption and diffusion of *n* -pentane in pellets of 5A zeolite, Ind. Eng. Chem. Res. 36 (1997) 493–500, https://doi.org/10.1021/ie960477c.
[48] R.M. Barrer, J.W. Sutherland, No Title, Proc. R. Soc. London. A (1956) 439.
[49] H.W. Habgood, Adsorptive and gas chromatographic properties of various cationic forms of zeolite X1, Can. J. Chem. 42 (1964) 2340–2350.
[50] S.Y. Zhang, O. Talu, D.T. Hayhurst, High-pressure adsorption of methane in zeolites NaX, MgX, CaX, SrX and BaX, J. Phys. Chem. 95 (1991) 1722–1726, https://doi.org/10.1021/j100157a044.

[51] S. Cavenati, C.A. Grande, A.E. Rodrigues, Adsorption equilibrium of methane, carbon dioxide, and nitrogen on zeolite 13X at high pressures, J. Chem. Eng. Data. 49 (2004) 1095–1101, https://doi.org/10.1021/je0498917.
[52] G. Maurin, S. Bourrelly, P.L. Llewellyn, R.G. Bell, Simulation of the adsorption properties of CH4 in faujasites up to high pressure: Comparison with microcalorimetry, Microporous Mesoporous Mater. 89 (2006) 96–102, https://doi.org/10.1016/j.micromeso.2005.09.024.
[53] M. Llano-Restrepo, Accurate fit and thermochemical analysis of the adsorption isotherms of methane in zeolite 13X, Adsorpt. Sci. Technol. 28 (2010) 579–600, https://doi.org/10.1260/0263-6174.28.7.579.
[54] M.A. Moreira, A.M. Ribeiro, A.F.P. Ferreira, A.E. Rodrigues, Cryogenic pressure temperature swing adsorption process for natural gas upgrade, Sep. Purif. Technol. 173 (2017) 339–356, https://doi.org/10.1016/j.seppur.2016.09.044.
[55] V. Mauer, C. Bläker, C. Pasel, D. Bathen, Energetic characterization of faujasite zeolites using a sensor gas calorimeter, Catalysts. 11 (2021) 98, https://doi.org/10.3390/catal11010098.
[56] J.A. Delgado, V.I. Águeda, M.A. Uguina, J.L. Sotelo, P. Brea, C.A. Grande, Adsorption and diffusion of H_2, CO, CH_4, and CO_2 in BPL activated Carbon and 13X zeolite: evaluation of performance in pressure swing adsorption hydrogen purification by simulation, Ind. Eng. Chem. Res. 53 (2014) 15414–15426, https://doi.org/10.1021/ie403744u.
[57] P. Brea, J.A. Delgado, V.I. Águeda, P. Gutiérrez, M.A. Uguina, Multicomponent adsorption of H_2, CH_4, CO and CO_2 in zeolites NaX, CaX and MgX, Evaluation of performance in PSA cycles for hydrogen purification, Micropor. Mesopor. Mater. 286 (2019) 187–198, https://doi.org/10.1016/j.micromeso.2019.05.021.
[58] Presidency of the Council of Ministers, Council of Ministers Resolution n.º 63/2020 - National Plan for Hydrogen Portogal, Diário Da República. (2020) 88. https://dre.pt/dre/detalhe/resolucao-conselho-ministros/63-2020-140346286.
[59] H.W. Langmi, A. Walton, M.M. Al-Mamouri, S.R. Johnson, D. Book, J.D. Speight, P. P. Edwards, I. Gameson, P.A. Anderson, I.R. Harris, Hydrogen adsorption in zeolites A, X, Y and RHO, J. Alloys Compd. 356–357 (2003) 710–715, https://doi.org/10.1016/S0925-8388(03)00368-2.
[60] K.S. Walton, M.B. Abney, M. Douglas LeVan, CO_2 adsorption in Y and X zeolites modified by alkali metal cation exchange, Micropor. Mesopor. Mater. 91 (2006) 78–84, https://doi.org/10.1016/j.micromeso.2005.11.023.
[61] A. Streb, M. Mazzotti, Adsorption for efficient low carbon hydrogen production: part 1—adsorption equilibrium and breakthrough studies for $H_2/CO_2/CH_4$ on zeolite 13X, Adsorption. 27 (2021) 541–558, https://doi.org/10.1007/s10450-021-00306-y.